communications engineering

Article

https://doi.org/10.1038/s44172-024-00254-9

Automatic renal carcinoma biopsy guidance using forward-viewing endoscopic optical coherence tomography and deep learning

Check for updates

Chen Wang [1], Haoyang Cui[2], Qinghao Zhang[1], Paul Calle [2], Yuyang Yan[1], Feng Yan[1], Kar-Ming Fung[3,4], Sanjay G. Patel[5], Zhongxin Yu[3,6], Sean Duguay[7], William Vanlandingham[7], Ajay Jain[4,8], Chongle Pan[2] ✉ & Qinggong Tang [1,4] ✉

Percutaneous renal biopsy is commonly used for kidney cancer diagnosis. However, the biopsy procedure remains challenging in sampling accuracy. Here we introduce a forward-viewing optical coherence tomography probe for differentiating tumor and normal tissues, aiming at precise biopsy guidance. Totally, ten human kidney samples, nine of which had malignant renal carcinoma and one had benign oncocytoma, were used for system evaluation. Based on their distinct imaging features, carcinoma could be efficiently distinguished from normal renal tissues. Additionally, oncocytoma could be differentiated from carcinoma. We developed convolutional neural networks for tissue recognition. Compared to the conventional attenuation coefficient method, convolutional neural network models provided more accurate carcinoma predictions. These models reached a tissue recognition accuracy of 99.1% on a hold-out set of four kidney samples. Furthermore, they could efficiently distinguish oncocytoma from carcinoma. In conclusion, our convolutional neural network-aided endoscopic imaging platform could enhance carcinoma diagnosis during percutaneous renal biopsy procedures.

Renal cancer is a disease characterized by the uncontrolled growth of kidney cells, resulting in the formation of tumor tissue. The lifetime risk of renal cancer was estimated to be ~2.02% in males and ~1.03% in females[1]. American Cancer Society projected approximately 81,800 new cases of renal cancer in the United States in 2023, including 52,360 males and 29,440 females, and 14,890 (9920 males and 4970 females) would die from it[1]. Renal cell carcinoma (RCC) is the most prevalent type of renal cancer, constituting approximately 95% of all renal cancer cases, and it has shown a consistent rise over the past few decades[2,3]. Accurate identification and diagnosis of renal tumor malignancy is critical for devising effective treatment plans. At present, percutaneous renal biopsy (PRB) is the most commonly used procedure to extract renal tissue for pathological analysis[4]. Since being proposed in 1951, PRB has been widely applied in the diagnosis and prognosis of kidney diseases[5]. It has been considered an effective method for the assessment of renal tumors in patients with RCC. During the PRB procedure, the patient is placed in a prone position. An exploratory needle is then inserted into the kidney to establish a path for the subsequent insertion of the biopsy needle[6]. The biopsy needle is employed to extract a tissue sample from the tumor. The obtained tissue sample is processed, analyzed, and classified as benign, malignant, or nondiagnostic for patients with RCC[7].

Despite being widely used for kidney disease diagnosis and renal tumor tissue evaluation, PRB still faces challenges in tissue localization. It has been reported that even with the assistance of a radiologist, approximately 92% of

[1]Stephenson School of Biomedical Engineering, University of Oklahoma, Norman, OK, USA. [2]School of Computer Science, University of Oklahoma, Norman, OK, USA. [3]Department of Pathology, University of Oklahoma Health Sciences Center, Oklahoma City, OK, USA. [4]Stephenson Cancer Center, University of Oklahoma Health Sciences Center, Oklahoma City, OK, USA. [5]Deparment of Urology, University of Oklahoma Health Sciences Center, Oklahoma City, OK, USA. [6]Children's Hospital, University of Oklahoma Health Sciences Center, Oklahoma City, OK, USA. [7]Department of Radiological Sciences, University of Oklahoma Health Sciences Center, Oklahoma City, OK, USA. [8]Department of Surgery, University of Oklahoma Health Sciences Center, Oklahoma City, OK, USA.
✉e-mail: cpan@ou.edu; qtang@ou.edu

PRBs required two or more attempts in order to accurately extract the targeted tissue[8]. More insertion attempts raise the likelihood of complications, including hematoma and infection[9,10]. Therefore, accurate guidance of needle insertion is of great importance for effective and safe renal carcinoma biopsy. Conventional imaging modalities have been employed for PRB needle guidance. Ultrasound has been utilized for needle placement guidance, effectively reducing the incidence rates of severe PRB complications over the past few decades[11,12]. Computed tomography (CT) has also been utilized in the diagnosis of metastatic lesions during percutaneous biopsy[13]. Three-dimensional cone-beam CT guidance has been documented as beneficial for the secure and effective determination of needle trajectory, as well as for performing biopsies on small renal masses[14]. Moreover, the guidance of PRB through magnetic resonance imaging (MRI) exhibits promising outcomes in precisely targeting the renal tumor and accurately locating the PRB needle tip, particularly in obese patients[15]. Although these macroscopic imaging methods, including ultrasound, CT, and MRI, are effective in needle trajectory determination, they cannot accurately identify tissue types ahead of the needle tip due to their limited spatial resolutions[16]. As a result, it was reported that ~10–20% of the biopsy results were non-diagnostic due to the limitation of imaging guidance of tumor location[16]. Hence, there is an unmet need for an imaging method capable of accurately identifying tissue types ahead of the PRB needle.

Optical coherence tomography (OCT) is a well-established imaging technique with micron-level spatial resolution[17]. Therefore, OCT has the potential to provide enhanced fine-scale visualization during PRB needle guidance. Moreover, OCT has already demonstrated feasibility in diagnosing renal masses, with the ability to differentiate renal tumor tissue from normal renal tissue based on distinct attenuation coefficients in OCT images[18–20]. OCT can also provide real-time imaging[21]. Therefore, we hypothesized that OCT can be used for real-time guidance of the PRB needle by detecting and identifying the renal tumor tissue. Here we have developed a forward-view OCT probe that incorporates gradient-index (GRIN) lenses functioning as a forward-viewing endoscope to enable tissue imaging ahead of the PRB needle. Our previous work successfully demonstrated the application of endoscopic OCT in percutaneous nephrostomy (PCN) guidance, accurately identifying various kidney tissues within pig models[22,23]. Hence, the OCT probe system holds promise in PRB needle guidance and renal tumor recognition.

Because visually identifying tissue from OCT images incurs a huge learning curve for radiologists and PRB operators, we have developed automatic imaging processing techniques, including tissue classification using attenuation coefficient and deep learning methods. Mapping optical attenuation coefficients has already been employed in distinguishing between cancerous and non-cancerous tissues[24]. Given that cancerous tissue tends to exhibit higher density in the imaging results, its attenuation coefficient typically surpasses that of normal tissues. Therefore, the attenuation coefficient can be a promising feature used for tumor tissue recognition during PRB needle guidance. Furthermore, deep learning has been demonstrated to be an effective approach in tissue classification and recognition for surgical guidance[23,25,26]. In this study, we have applied convolutional neural networks (CNNs) for the automatic identification of carcinoma from normal tissue and oncocytoma. The performance of these methods was benchmarked for renal tissue classification and tumor diagnosis.

Materials and methods

Experimental setup

We constructed our forward-viewing OCT probe based on a swept-source OCT system[23,26,27]. The light source utilized was a 1300 nm swept-source laser with a bandwidth of 100 nm. The scanning rate of our system reached 200 kHz. As illustrated in Fig. 1A, the light was initially divided using a fiber coupler (FC) into two distinct paths: one directed with 97% of power toward

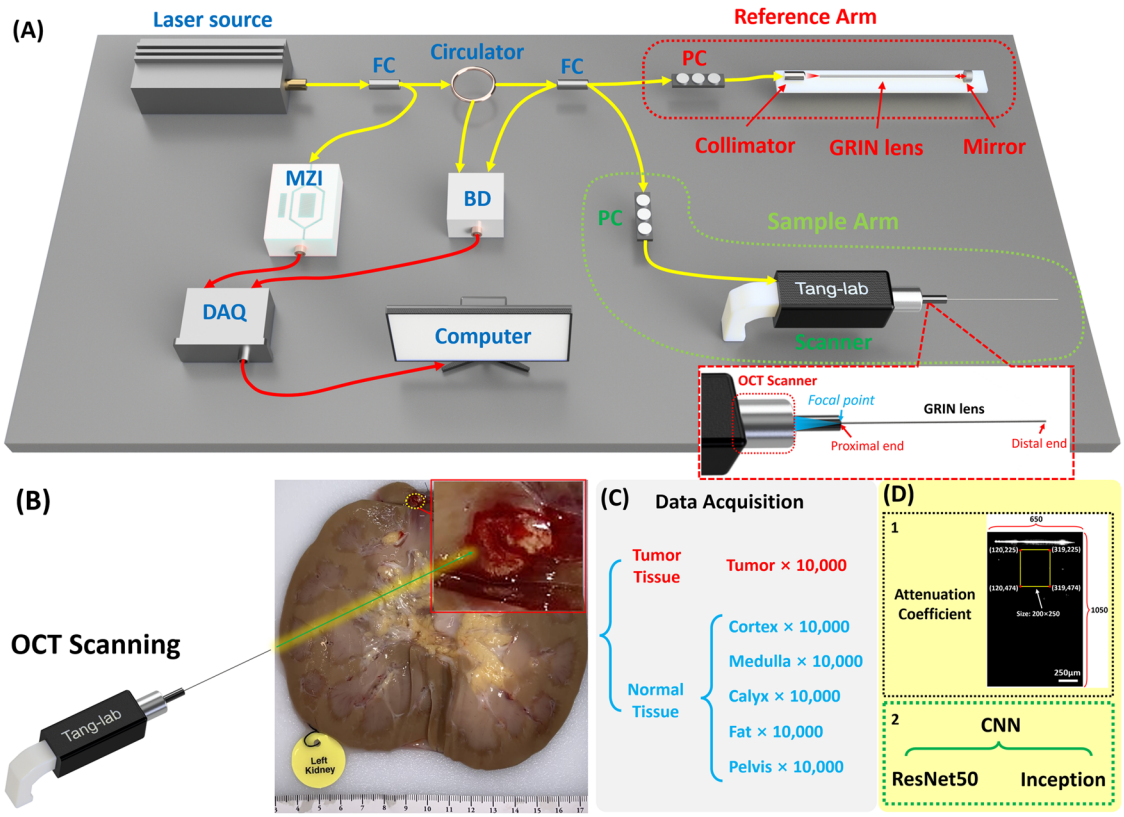

Fig. 1 | Experimental setup of the endoscopic OCT system and the data collection/processing. A Schematic of the forward-viewing OCT probe. **B** Picture of the human kidney with renal carcinoma. **C** DAQ of renal tumor tissue and normal tissue. **D** The attenuation coefficient and two CNN architectures were used for tissue classification. FC fiber coupler, PC polarization controller, MZI Mach–Zehnder interferometer, BD balanced detector, DAQ data acquisition.

a circulator for the OCT imaging, and the other with 3% power directed to a Mach–Zehnder interferometer (MZI) to initiate the sampling process. Upon traversing the circulator, the laser underwent another division through another FC into the reference arm and sample arm. Subsequently, the light reflected by the mirror in the reference arm and the light backscattered by the tissue in the sample arm converged, generating an interference signal. This signal was then denoised using a balanced detector (BD), acquired by the data acquisition (DAQ) board, and finally processed and visualized on a computer. Polarization controllers (PC) were employed in both arms to reduce background noise.

In PRB procedures, 14 gauge (G) or 16 G biopsy needles are commonly used[28]. To assess feasibility, we employed GRIN lenses with a diameter of 1.3 mm and length of 138.0 mm, allowing them to be accommodated within the 14 G or 16 G biopsy needles. These GRIN lenses possess a refractive index distribution that varies perpendicular to the optical axis, facilitating effective image transmission from one end to the other[29]. The GRIN lens in our system was featured with a pitch length of four integers, thus enabling the direct relay of laser profiles or images from one end to the other[22,23].

In the sample arm, the proximal end of the GRIN lens was precisely positioned at the focal point of the scanner lens, while the distal end was in contact with the sample. Consequently, the laser profile was directly transmitted from the proximal surface to the sample. Simultaneously, spatial information from the distal surface (tissue sample) of the GRIN lens, transmitted to the proximal surface, was further captured by the OCT scanner. Additionally, another GRIN lens was situated in the reference arm to counteract light dispersion. Our system features an axial resolution of approximately 11 μm and a lateral resolution of around 20 μm. It provides a sensitivity of 92 dB and covers a field of view (FOV) of approximately 1.25 mm in diameter, rendering it well-suited for our intended application.

Data collection

The study was approved by the University of Oklahoma Institutional Review Board (Study number: 12462). Written informed consent was obtained by Lifeshare of Oklahoma. Patient demographics were collected upon obtaining consent. For our dataset, we utilized nine human kidney samples with renal carcinoma. OCT images of carcinoma tissue and different normal tissues were imaged by our OCT probe. Furthermore, to compare benign renal tumors against malignant renal carcinoma in this study, we conducted OCT imaging on one kidney sample with oncocytoma, which is a well-defined benign solid tumor arising from the proximal renal tubule[30]. To keep the organ as fresh as possible, all the kidney samples were preserved by hypothermic machine perfusion., and we started the experiment as soon as the sample was acquired.

Figure 1B illustrates one of the kidney samples with carcinoma, clearly showcasing the tumor tissue alongside other normal renal tissues including cortex, medulla, calyx, fat, and pelvis. To emulate a practical biopsy procedure during the experiment, we carefully inserted the OCT probe into different renal tissue types, applying controlled force to compress the tissue. OCT image acquisition was successfully performed in the final.

For quantitative identification of tumor tissue, we utilized both conventional methods, involving the calculation of attenuation coefficients, and deep learning techniques for automated recognition of renal tissue types. To train the deep learning model, we obtained a dataset of 10,000 OCT images from the tumor and five different normal renal tissues in each kidney sample, respectively (Fig. 1C). The size of all output images was set as lateral × depth: 650 × 1050 (X × Z: 1.30 × 2.10 mm^2), so each result covered the same FOV for the attenuation coefficient method and CNN process (Fig. 1D). For each method (attenuation coefficient and CNN), data from five kidney samples with carcinoma were used to train and benchmark the model by nested cross-validation, and the other four kidney samples with carcinoma were used in a hold-out set to independently benchmark the prediction performance. 10,000 oncocytoma OCT images were further tested to compare the biological features of oncocytoma with carcinoma.

Attenuation coefficient method for tissue recognition

Our OCT findings provided in-depth structural insights into renal tissues. The attenuation coefficient serves as a crucial parameter, signifying the decrease in signal intensity observed in OCT images as depth increases[31]. In structural OCT images, the imaging intensity reflects the backscattering level of the tissue sample, so different attenuation coefficients demonstrate different tissue features and can be used for tissue classification. The use of attenuation coefficient for cancer detection has been extensively documented[32–34]. Compared to normal tissues, cancerous tissue is typically denser thus its imaging signal value attenuated faster in the vertical direction and is represented by a higher attenuation coefficient. The attenuation coefficient of each A-scan can be extracted and used to generate a spatial attenuation coefficient distribution, which helps visually distinguish tumor and normal tissues[24].

Here we used Beer–Lambert law to describe the structural OCT intensity signals in depth as follows:

$$I_{(z)} = I_0 e^{-2\mu z} \tag{1}$$

where I_0 represents the initial incident light intensity, μ is the attenuation coefficient value which represents the decay rate, and z is the depth[35]. Thus, μ can be described as:

$$\mu = -\frac{1}{2} \cdot \frac{d \log I_{(Z/0)}}{d_z} \tag{2}$$

$I_{(Z/0)}$ is the ratio of recorded OCT intensity in depth to the initial incident light intensity. The intrinsic optical attenuation coefficient was calculated according to the slope of OCT intensity in a 250-pixel depth window and then averaged in a 200-pixel width region as shown in Fig. 1D.

CNN methods for tissue identification

Two CNN architectures, ResNet50 and InceptionV3, were evaluated. ResNet50 has ~25.6 million parameters and InceptionV3 has ~22 million parameters. Five kidney samples with carcinoma were used to develop the CNN architectures. We used nested 4-fold cross-validation and 5-fold cross-testing procedure[23], in which each iteration rotated three kidneys to the training dataset, one kidney to the validation dataset, and one kidney to the test dataset. This division enabled us to obtain a more accurate estimation of the generalization error, as every kidney was included in the test dataset once. Early stopping was implemented with a patience of 20. The optimizer used for the training was stochastic gradient descent with Nesterov accelerated gradient, utilizing a momentum value of 0.9 and a learning rate of 0.01. Additionally, the learning decay rate was set to be 0.1. The average epoch count from the cross-validation folds was subsequently employed to train the model intended for use on the test dataset. The test performances of the obtained models were benchmarked using the 5-fold cross-testing.

A final CNN model was trained using all five kidneys included in the nested cross-validation with the identified optimum hyperparameters. The performance of the final CNN model was benchmarked using a separate hold-out set which contains four additional kidney samples with carcinoma. Furthermore, one oncocytoma sample was also used to test the capability of the final CNN model for distinguishing oncocytoma from carcinoma. The classification performance was measured using four metrics, including accuracy, precision, recall, and F_1 score as defined below:

$$\text{Accuracy} = (\text{TP} + \text{TN})/(\text{TP} + \text{FP} + \text{TN} + \text{FN}) \tag{3}$$

$$\text{Precision} = \text{TP}/(\text{TP} + \text{FP}) \tag{4}$$

$$\text{Recall} = \text{TP}/(\text{TP} + \text{FN}) \tag{5}$$

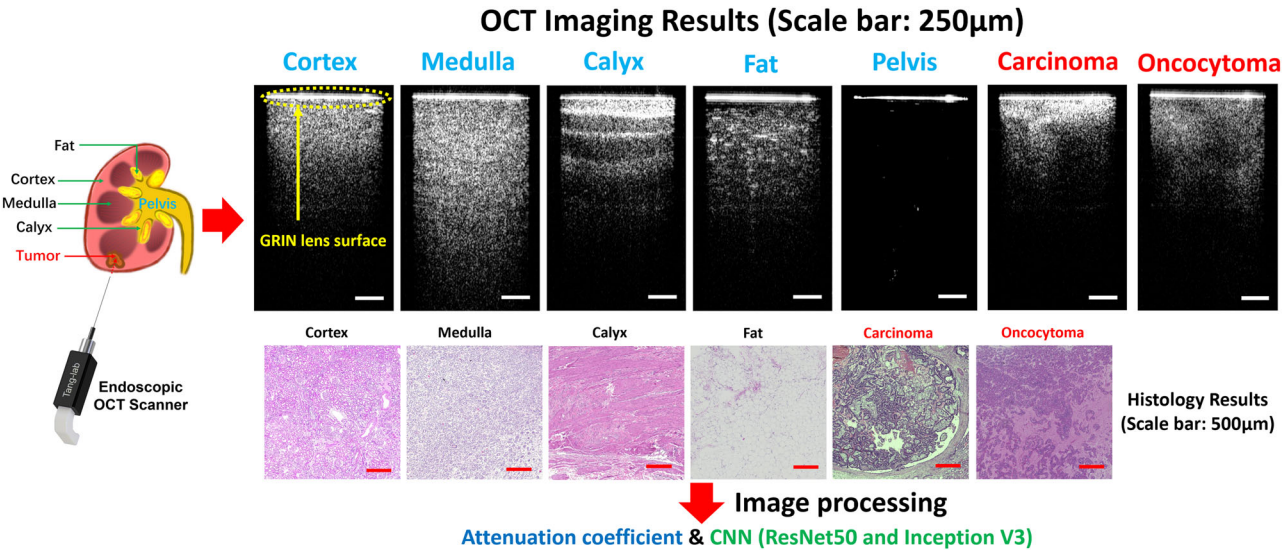

Fig. 2 | OCT imaging results of normal renal tissues, carcinoma, and oncocytoma (scale bar: 250 μm). Corresponding histology results (scale bar: 500 μm).

$$F_1\ \text{score} = 2 \cdot \frac{\text{Precision} \cdot \text{Recall}}{\text{Precision} + \text{Recall}} = \frac{\text{TP}}{\text{TP} + \frac{1}{2}(\text{FP} + \text{FN})} \quad (6)$$

where TP is true positive, FP is false positive, TN is true negative, and FN is false negative.

To interpret the prediction of deep learning models[36,37], GradCAM[38] was used to generate pixel saliency heatmaps. One of the five kidneys' images was used to generate the heatmaps for both CNN models: InceptionV3 and ResNet50. For example, all images of the cortex from the chosen kidney were utilized. We calculated the sum of the corresponding pixel points of the images, then the sum was divided by the number of total images used, resulting in an average heatmap image of the cortex. The same practice applied to the rest of the tissue types.

Reporting summary

Further information on research design is available in the Nature Portfolio Reporting Summary linked to this article.

Results

Imaging results of renal tumor and normal tissues

Figure 2 illustrates the OCT imaging results obtained through our OCT probe, demonstrating malignant renal carcinoma, benign renal oncocytoma, and five distinct normal renal tissue types. Two-dimensional cross-sectional OCT images of these tissues demonstrate different structural features. The corresponding histology results are also shown in Fig. 2. The renal pelvis is the cavity for collecting urine, hence there is no histology result for it.

In the OCT results, there is a bright line on the top (pointed by a yellow arrow) which corresponds to the surface of the GRIN lens. The intensity signal distributions of both the cortex and medulla are relatively homogeneous, although the imaging depth of the medulla surpasses that of the cortex. Calyx exhibits alternately shaded stripes, as a result of its transitional epithelium and fibrous tissue composition. Fat presents the darkest pattern, accompanied by bright dots characteristic of adipocytes. We injected synthetic urine into the pelvis tied the ureter during the experiment and inserted the probe into the pelvis for imaging. As an empty space for collecting urine, the pelvis has no tissue signal under the GRIN lens surface. The renal carcinoma, being the pivotal tissue type for identification during PRB, showcases the shallowest imaging depth while presenting the highest brightness among all OCT results. Its structural features exhibit irregularities. Compared to carcinoma, the overall imaging density of oncocytoma is relatively lower, while there are still clear irregular structural features. From the corresponding histology results, these tissues showed different tissue structures and distributions and correlated well with their OCT results. Different normal renal tissues and the two types of tumor tissues can be categorized based on their distinctive OCT imaging features. As a result, our endoscopic OCT probe has the potential to assist in the recognition of tissue types ahead of the needle during PRB procedures.

Classification using the attenuation coefficient method

We first assessed the performance of the attenuation coefficient method in distinguishing renal tumors and normal tissues. The attenuation coefficient did not work for the pelvis, because the values of most pixels were zero and the logarithm could not be calculated. Therefore, only tumor tissue and the other four normal tissue types were tested using the attenuation coefficient method.

This study involved the processing of a total of 50,000 OCT images from each of the five cross-testing samples (after removing the pelvis category) with each tissue type contributing 10,000 images. The performance of the results was benchmarked first using the cross-testing procedure and then using a hold-out set containing five additional kidney samples (four renal carcinomas and one benign renal oncocytoma). Among the five cross-testing samples, four of them were randomly selected as the training dataset, while the remaining kidney served as the test dataset. To calculate the attenuation coefficient, the region of interest (ROI) window was selected to be 200 × 250 pixels for each OCT image. The ROIs were chosen from the central sections of the images and the coordinate of the area is selected in the top middle position which includes most tissue information (Fig. 1D). The mean value of all the attenuation coefficient results from every vertical direction was used as the attenuation coefficient level for each OCT image.

Figure 3 displays the attenuation coefficient distributions for the five tissue types (four normal renal tissues and renal carcinoma). Firstly, considering cortex, medulla, calyx, and fat are all normal tissues, these four types were initially consolidated into a single classification. In this testing, all the tumor tissue images from five samples (50,000 images in total) were utilized. To make the number of normal tissue images equal to the number of tumor images, we randomly selected 2500 images from each normal tissue in every sample (2500 images × 4 tissue types × 5 samples = 50,000 images). In general, the tumor tissue and the normal tissues displayed distinctive distribution characteristics, thereby enabling a clear differentiation between tumor and normal tissues as shown in Fig. 3A. Normal distributions were fitted to the attenuation coefficient distributions as shown in Fig. 3A. To quantify the separation of the tumor from normal tissues, the cross point (blue dot) of two curves was chosen as a threshold and used to evaluate the

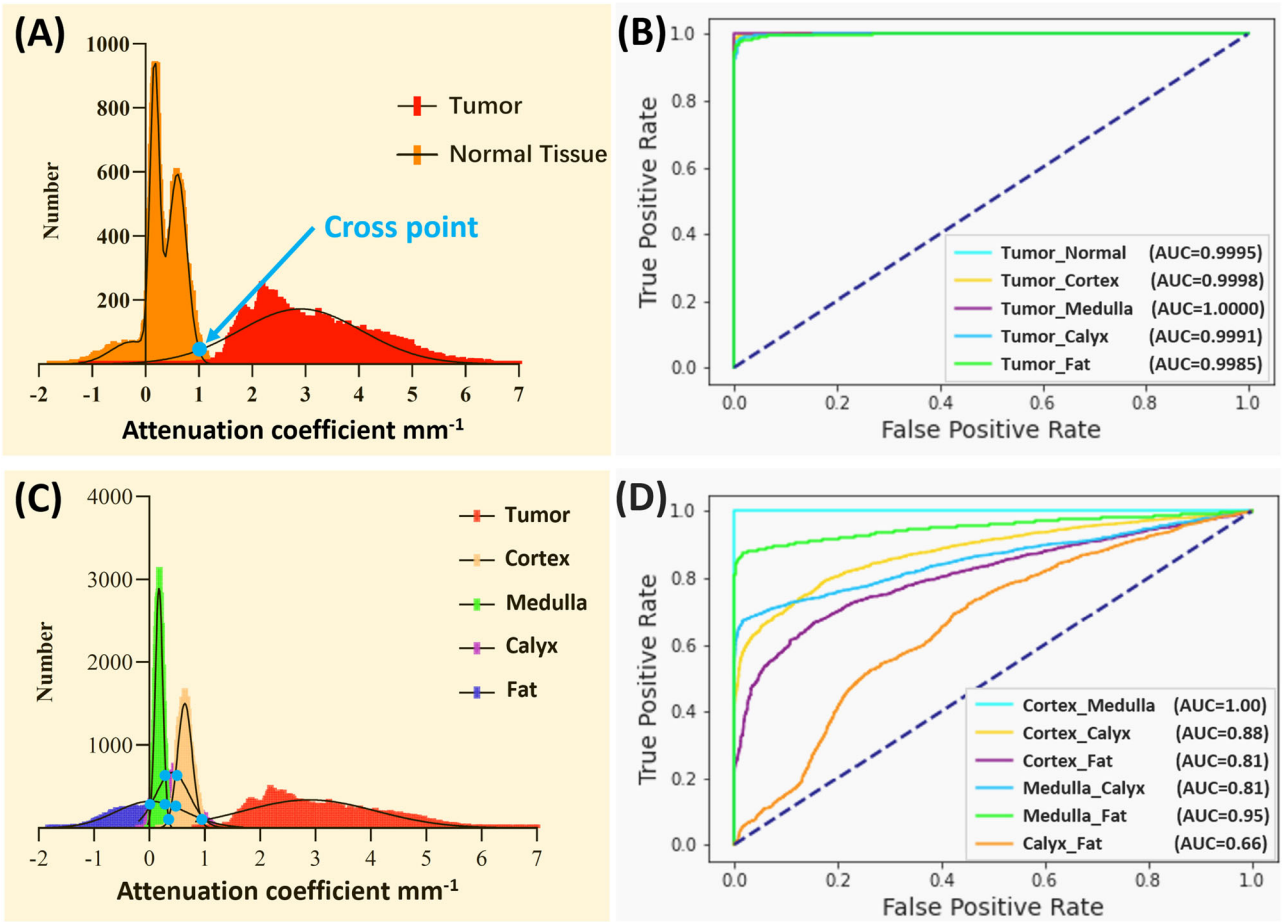

Fig. 3 | Distributions and prediction results of the five sample datasets using attenuation coefficient. A Attenuation coefficient distribution results between normal tissue and tumor tissue. **B** ROC curves of the classification with attenuation coefficient between tumor tissue and other tissues. **C** Attenuation coefficient distribution results of all five tissue types. **D** ROC curves of the classification with attenuation coefficient among different normal tissues. ROC receiver operating characteristic.

accuracy. The receiver operating characteristic (ROC) curves were shown between tumor and normal renal tissues in Fig. 3B. The area under the ROC curves (AUC) (Tumor_Normal) was 99.95%, which validated the tumor recognition accuracy based on attenuation coefficients.

We then evaluated the classification of the renal tissue types by using 10,000 OCT images from each of the five samples (50,000 images in total). The attenuation coefficient distributions are shown in Fig. 3C. To quantify the separation of the tumor from each normal tissue (i.e., tumor vs cortex, tumor vs medulla, tumor vs calyx, and tumor vs fat), the cross point (blue dot) of two curves was again chosen as threshold and used to evaluate the accuracy. The AUCs for differentiating the tumor tissue from each normal renal tissue were all over 99.85% (Fig. 3B), which further proved the tumor recognition capacity of using attenuation coefficients.

However, different normal renal tissues were difficult to classify using the attenuation coefficient method. The AUCs were 100% for cortex vs medulla, 88% for cortex vs calyx, 81% for cortex vs fat, 86% for medulla vs calyx, 95% for medulla vs fat, and only 66% for calyx vs fat (Fig. 3D). The confusion matrix for multi-class classification was further shown in Table 1A, and the corresponding prediction results were shown in Table 1B. Tumor demonstrated high recognition performance, with 98.19% accuracy, 91.85% precision, 99.83% recall, and 95.67% F_1 score. However, normal tissue recognition was challenging, especially for calyx (78.77% accuracy, 43.18% precision, 19.47% recall, and 26.84% F_1 score). The needle's precise placement can enhance surgical efficiency and overall effectiveness. The present results primarily demonstrated the promise of tumor recognition, but the performance in identifying other normal kidney tissues still needed improvement. In particular, the attenuation coefficient methods misclassified over 500 images of calyx as tumor tissue, causing potential sampling errors. The prediction results from each of the five samples are included in Supplementary Tables 1–5.

Further benchmarking with the hold-out set containing four kidney samples with carcinoma was conducted and the corresponding results were demonstrated in Table 2. Similar to previous cross-testing results, carcinoma provided high accuracy and recall of 93.29% and 99.74% respectively. However, the precision and F_1 score just reached 74.96% and 85.60%. This decrease can be attributed to the fact that over 3,000 calyx images were incorrectly predicted as carcinoma. Moreover, the prediction of normal tissue remained unsatisfactory. Therefore, the attenuation coefficient, as a conventional tool, is not an effective method for renal carcinoma recognition during PRB. The prediction results of each sample in the hold-out set are included in Supplementary Tables 6–9.

In addition, we tested 10,000 oncocytoma OCT images using attenuation coefficient, with the results shown in Table 3. It demonstrated that over 60% of the oncocytoma imaging results were predicted as carcinoma and over 30% were misclassified as cortex. This further indicated that the attenuation coefficient was not effective in distinguishing between oncocytoma and carcinoma.

Tissue recognition results using CNN

The recognition of kidney tissues using the ResNet50 and InceptionV3 CNNs was evaluated using cross-testing on the five nested cross-validation kidney samples with carcinoma. The ROC curves and pixel saliency

Table 1 | Statistical results of the five sample datasets using attenuation coefficient

(A)						
Tissue		**Prediction of five samples using attenuation coefficient**				
		Cortex	**Medulla**	**Calyx**	**Fat**	**Carcinoma**
True	Cortex	9145	14	723	0	118
	Medulla	3	9154	756	87	0
	Calyx	4326	2820	1947	347	560
	Fat	1895	1872	1083	4942	208
	Carcinoma	17	0	0	0	9983

(B)				
Tissue	**Accuracy**	**Precision**	**Recall**	**F_1 score**
Cortex	85.81%	59.44%	91.45%	72.05%
Medulla	88.90%	66.05%	91.54%	76.73%
Calyx	78.77%	43.18%	19.47%	26.84%
Fat	89.02%	91.93%	49.42%	64.28%
Carcinoma	98.19%	91.85%	99.83%	95.67%

A: confusion matrix. B: prediction results: accuracy; precision; recall; and F_1 score of different tissue types.

Table 2 | Statistical testing results of the hold-out set with an additional four kidney samples using attenuation coefficient

(A)						
Tissue		**Testing of the hold-out set using attenuation coefficient**				
		Cortex	**Medulla**	**Calyx**	**Fat**	**Carcinoma**
True	Cortex	7418	306	2170	0	106
	Medulla	6	9225	756	13	0
	Calyx	2452	2612	1228	604	3104
	Fat	1007	1418	775	6679	121
	Carcinoma	7	4	2	13	9974

(B)				
Tissue	**Accuracy**	**Precision**	**Recall**	**F_1 score**
Cortex	87.89%	68.12%	74.18%	71.02%
Medulla	89.77%	68.01%	92.25%	78.29%
Calyx	75.05%	24.90%	12.28%	16.45%
Fat	92.10%	91.38%	66.79%	77.17%
Carcinoma	93.29%	74.96%	99.74%	85.60%

A: confusion matrix. B: performance metrics.

Table 3 | Prediction results of oncocytoma tissues using attenuation coefficient

		Testing of oncocytoma sample predictions by attenuation coefficient				
		Cortex	**Medulla**	**Calyx**	**Fat**	**Carcinoma**
True	Oncocytoma	3087	185	484	197	6047

heatmaps are shown in Fig. 4. The confusion matrixes and performance metrics are shown in Table 4.

The ResNet50 CNN yielded a tumor recognition accuracy of 99.51%. For normal tissue recognition, the prediction accuracies were 98.96% for the cortex, 99.78% for the medulla, 99.09% for the calyx, 99.27% for fat, and 99.95% for the pelvis. Most of the tumor sample misclassifications (123 of 134) were erroneously categorized as cortex. None of the cortex, medulla, and fat images were predicted to be tumors, and 1.48% of the calyx images were falsely predicted as tumors. The InceptionV3 CNN reached 99.48% tumor prediction accuracy. The accuracies for normal tissue classification were 99.58% for the cortex, 99.88% for the medulla, 99.27% for the calyx, 99.65% for fat, and 99.95% for the pelvis. Calyx recognition has the lowest accuracy, and 0.02% of tumor samples were erroneously categorized as calyx, which is different from the ResNet50 model. Both ResNet50 and InceptionV3 achieved >99.9% ROC AUC for all tissues.

InceptionV3 outperformed ResNet50 in overall precision for the classification of the normal renal tissues, with a slightly lower precision in the tumor classification. All normal tissues and tumor results using InceptionV3 have higher recalls than ResNet50 except for calyx. Additionally, calyx provides the lowest F_1 scores in both models, but the overall performances for carcinoma are still promising (both > 98%).

The average pixel importance heatmaps of all the images from the two models are shown in Fig. 4. These heatmaps highlighted the regions important for the models to distinguish different tissue types. The narrow area below the GRIN lens surface line was important for tumor recognition. The important area for pelvis recognition included a narrow part on the top and a wide area on the bottom. Heatmaps of the other four tissues all highlighted the top half of the images with strong signals. The important areas used by ResNet50 were sparser and wider than those used by InceptionV3. This could be attributed to the fact that ResNet50's feature map was

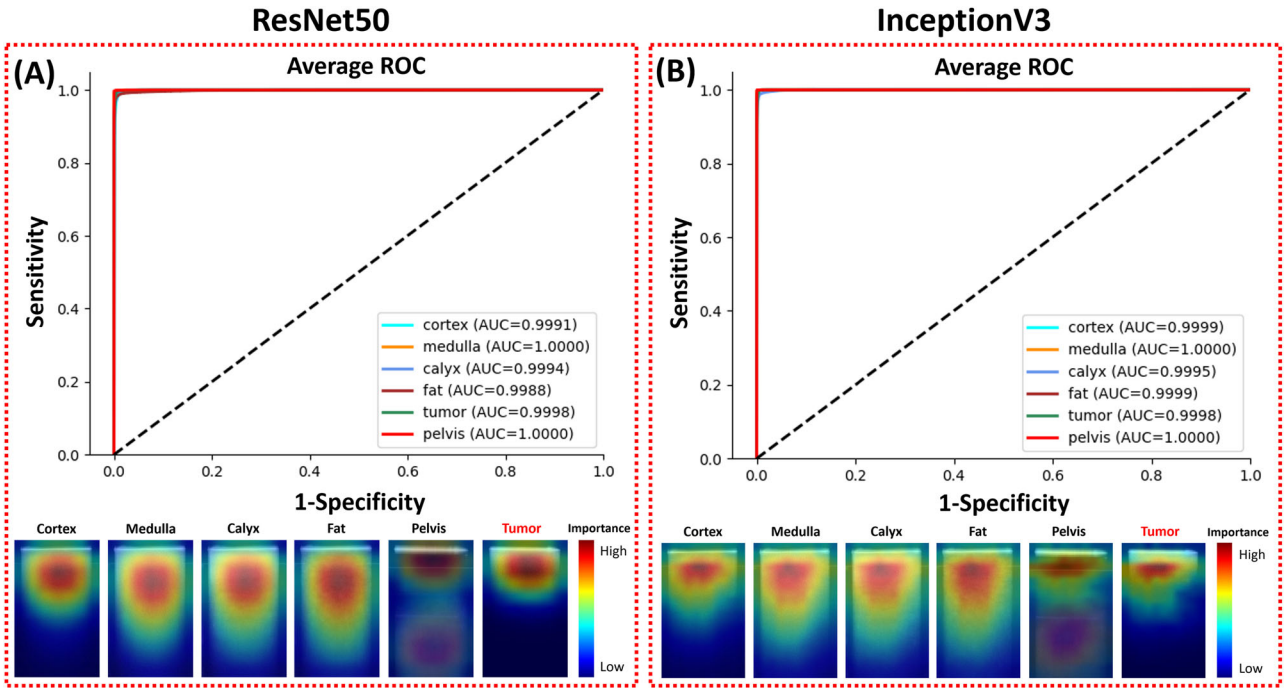

Fig. 4 | Prediction results of the two CNN models. ROC curves and pixel importance heatmaps of (**A**) ResNet50, and (**B**) InceptionV3 are demonstrated. ROC receiver operating characteristic, AUC area under the curve.

more focused and localized within each residual block than InceptionV3, so it could capture fine-grained details in the images at the pixel level.

For the performance of nested cross-validation between the two models, the average accuracies across five kidney samples with InceptionV3 and ResNet50 for predicting all tissue types were 98.26% and 97.32%, respectively. The overall prediction accuracies of the two models were close, with InceptionV3 being higher marginally. In addition, the inference time was 18 ms per image for ResNet50, and 11 ms per image for InceptionV3. Thus, to make the prediction more efficient, we utilized InceptionV3 as the final CNN model for the hold-out testing. The experiment was performed using a hold-out set with four additional samples with carcinoma, with the results displayed in Table 5. The final CNN model made erroneous carcinoma predictions at a rate of 0.35% to fat and 1.96% to pelvis, respectively. For F_1 scores of all tissue types in the prediction with the hold-out set, they outperformed the nested cross-validation results demonstrated in Fig. 4B.

To test the feasibility of distinguishing oncocytoma from carcinoma, we further tested the 10,000 oncocytoma OCT images using the final CNN model. The predicted results are shown in Table 6. On average, the final CNN model exhibited a misrecognition rate of oncocytoma as carcinoma at 2.24%. Most of the oncocytoma images were misclassified as cortex and fat. The results proved that our final CNN model could effectively distinguish oncocytoma from carcinoma.

Discussion

Although PRB is the most commonly performed procedure for evaluating renal tissue, it remains a challenge even for experienced urologists to precisely extract carcinoma tumor tissue with minimal sampling error. In this study, we tested the feasibility of using a forward-viewing OCT probe for RCC detection on ex vivo human kidneys. In total, ten human kidney samples, nine of which have malignant renal carcinoma and one has benign renal oncocytoma, were utilized in our experiments to validate our approach. The two types of renal tumor tissues and different normal renal tissues, including cortex, medulla, calyx, renal fat, and pelvis were all included to evaluate the recognition accuracy of our system. We applied the probe to these tissues and obtained their OCT images. The OCT images of different renal tissues could be classified based on their distinct imaging characteristics. Moreover, the OCT probe's dimensions were designed to fit inside the PRB needle's hollow bore, enabling seamless integration without introducing any additional invasiveness. Under clinical settings, our OCT probe can image the tissue in front of the PRB needle in real-time, effectively identifying the tissue type at the needle's tip.

To automate the process of tissue identification, we utilized and compared two classification methods in our study: attenuation coefficient and deep learning. The attenuation coefficient method has been widely used in OCT-based cancer diagnosis, including breast cancer[33], prostate cancer[39], bladder cancer[34], colon cancer[40], etc. Renal mass diagnosis using OCT was also reported, and it exhibited highly promising outcomes in predicting RCC[41]. For the classification task, we utilized the data from five carcinoma samples to train and benchmark the models using cross-testing and employed a hold-out set for further testing. We first evaluated the attenuation coefficient for the identification of tumors and normal tissues. Discrimination of tumors from normal tissues was promising with an accuracy of 98.19% in cross-testing, and 93.29% in the hold-out testing. Although the results were generally favorable, misrecognition still happened. Additionally, relying solely on the attenuation coefficient proved challenging when it came to distinguishing between different types of normal renal tissues. The classification accuracy results were not satisfactory, particularly for the calyx prediction accuracy which fell below 80% in both testing procedures. In addition, we tested the model performance for distinguishing between benign and malignant renal tumors. Over 60% of the oncocytoma data were erroneously predicted as carcinoma, further indicating that the attenuation coefficient was not an efficient tool in renal tissue recognition.

Accurate identification of normal renal tissues prior to biopsy needle insertion played a pivotal role in precisely tracking the needle's location and avoiding sampling error. To address this critical need, we further evaluated the deep learning methods in our study. Specifically, we employed two well-established CNN architectures, ResNet50 and InceptionV3, both of which demonstrated robust performance in tumor recognition and the classification of various normal renal tissues.

Table 4 | Statistical cross-validation results of the five sample datasets using two CNN models

(A)

Tissue		Performance benchmarking by nested cross-validation using ResNet50					
		Cortex	Medulla	Calyx	Fat	Pelvis	Carcinoma
True	Cortex	9875	75	23	27	0	0
	Medulla	43	9956	1	0	0	0
	Calyx	136	15	9553	148	0	148
	Fat	199	0	56	9745	0	0
	Pelvis	0	0	21	0	9969	10
	Carcinoma	123	0	0	9	2	9866

(B)

Prediction cross-validation results of ResNet50

Tissue	Accuracy	Precision	Recall	F_1 score
Cortex	98.96%	95.16%	98.75%	96.92%
Medulla	99.78%	99.10%	99.56%	99.33%
Calyx	99.09%	98.95%	95.53%	97.21%
Fat	99.27%	98.15%	97.45%	97.80%
Pelvis	99.95%	99.98%	99.69%	99.83%
Carcinoma	99.51%	98.43%	98.66%	98.54%

(C)

Tissue		Performance benchmarking by nested cross-validation using InceptionV3					
		Cortex	Medulla	Calyx	Fat	Pelvis	Carcinoma
True	Cortex	9964	1	1	34	0	0
	Medulla	15	9978	7	0	0	0
	Calyx	69	38	9639	0	0	254
	Fat	121	0	30	9822	0	27
	Pelvis	0	11	15	1	9973	0
	Carcinoma	10	0	22	0	0	9968

(D)

Prediction cross-validation results of InceptionV3

Tissue	Accuracy	Precision	Recall	F_1 score
Cortex	99.58%	97.89%	99.64%	98.76%
Medulla	99.88%	99.50%	99.78%	99.64%
Calyx	99.27%	99.22%	94.39%	96.74%
Fat	99.65%	99.64%	98.22%	98.92%
Pelvis	99.95%	100.00%	99.73%	99.86%
Carcinoma	99.48%	97.26%	99.68%	98.64%

Confusion matrices and performance metrics of A, B: ResNet50 and C, D: InceptionV3

In cross-testing using the five carcinoma samples, InceptionV3 achieved tumor recognition rates of 99.48%, which surpassed the performance of the attenuation coefficient method. Equally impressive was the accuracy in normal tissue recognition, with rates consistently exceeding 99% across all tissue types. ROC curves for both models showed AUC values consistently exceeding 99.9%. This observation underscores the effectiveness of the CNN-based approach for the classification of different normal renal tissues compared to the attenuation coefficient method. The performance of these models can be attributed, in part, to their substantial parameter sets. ResNet50 features 25.6 million and InceptionV3 features 22 million parameters, respectively, in contrast to the single parameter employed by the attenuation coefficient method. All computations were conducted on a server equipped with two NVIDIA RTX A6000 graphics cards. The cross-validation required an average of 1435 min per fold. The average inference time over 320 images was 18 ms per image for ResNet50 and 11 ms per image for InceptionV3. For a regular OCT workstation with P1000 GPU, the inference time was 0.27 s for ResNet and 0.17 s for InceptionV3 per image, which can be still considered 'real-time' tissue classification. To further facilitate clinical translation, future research could investigate the use of more compact architectures with faster processing times, while still preserving the integrity of performance. Theoretically, CNN architectures with fewer trainable parameters or less depth will reduce the processing time and improve efficiency. For instance, we will consider using pretrained EfficientNet or VGG16 architectures, to reduce the training and inference time. The prediction results from the hold-out set containing four additional carcinoma samples revealed promising generalization capability of the final CNN model as it showed higher F_1 scores for the majority of the tissue types compared to the results in previous cross-testing. Therefore, the final CNN model trained with the architecture of InceptionV3 could be considered a suitable one for carcinoma recognition during PRB using endoscopic OCT in our study. Furthermore, the final CNN model was

Table 5 | Statistical testing results of the hold-out set with an additional four kidneys using the final production CNN model

(A)							
Tissue		**Testing of the hold-out set using the final CNN model**					
		Cortex	**Medulla**	**Calyx**	**Fat**	**Pelvis**	**Carcinoma**
True	Cortex	9997	0	0	3	0	0
	Medulla	0	10000	0	0	0	0
	Calyx	161	1	9697	90	0	51
	Fat	0	0	32	9968	0	0
	Pelvis	0	0	0	0	10000	0
	Carcinoma	0	0	0	35	196	9796

(B)				
Performance metrics of the hold-out set testing using the final CNN model				
Tissue	**Accuracy**	**Precision**	**Recall**	**F_1 score**
Cortex	99.73%	98.42%	99.97%	99.19%
Medulla	100.00%	99.99%	100.00%	100.00%
Calyx	99.44%	99.67%	96.97%	98.30%
Fat	99.73%	98.73%	99.68%	99.20%
Pelvis	99.67%	98.33%	100.00%	99.16%
Carcinoma	99.53%	99.48%	97.96%	98.71%

A: confusion matrix and B: performance metrics.

Table 6 | Predictions of oncocytoma by the final CNN model

		Testing of oncocytoma sample predictions by the final CNN model					
		Cortex	**Medulla**	**Calyx**	**Fat**	**Pelvis**	**Carcinoma**
True	Oncocytoma	9215	0	0	553	8	224

further tested using a renal oncocytoma sample. Although no renal oncocytoma images were involved in the training procedure, it exhibited strong performance in differentiating between benign oncocytoma and malignant carcinoma tumors, further demonstrating the capability for accurately recognizing renal carcinoma.

Conclusion

We tested the feasibility of employing an endoscopic OCT probe for the diagnosis of renal cancer. Renal tumors and normal kidney tissues can be distinguished based on their OCT images. To automate this process, we utilized both attenuation coefficient and deep learning methods for renal tissue recognition. The attenuation coefficient enabled the differentiation between tumor and normal tissues, while the CNN method further classified tumor tissue as well as different normal renal tissues accurately. It is worth noting that CNN also provided better performance for distinguishing benign and malignant renal tumors. By combining the deep learning approach with the forward-viewing OCT probe, we envision the creation of a precise imaging guidance tool for the PRB procedure. Moreover, our system can complement the established clinical PRB guiding methods, including ultrasound, fluoroscopy, and CT by providing high-resolution images in front of the PRB needle in real-time.

Data availability

The data used in our deep learning training and testing work is available from https://zenodo.org/records/12170637.

Code availability

The code used in this study can be found at: https://github.com/thepanlab/prb_guidance_paper.

Received: 10 November 2023; Accepted: 22 July 2024;
Published online: 02 August 2024

References

1. American Cancer Society (2022) *Key Statistics About Kidney Cancer.* https://www.cancer.org/cancer/kidney-cancer/about/key-statistics.html.
2. Levi, F. et al. The changing pattern of kidney cancer incidence and mortality in Europe. *BJU Int.* **101**, 949–958 (2008).
3. Ferlay, J. et al. Cancer incidence and mortality patterns in Europe: estimates for 40 countries and 25 major cancers in 2018. *Eur. J. Cancer* **103**, 356–387 (2018).
4. Whittier, W. L. Complications of the percutaneous kidney biopsy. *Adv. Chronic Kidney Dis.* **19**, 179–187 (2012).
5. Iversen, P. & Brun, C. Aspiration biopsy of the kidney. *Am. J. Med.* **11**, 324–330 (1951).
6. Kark, R. M. & Muehrcke, R. C. Biopsy of kidney in prone position. *Lancet* **1**, 1047–1049 (1954).
7. Tsivian, M. et al. Small renal mass biopsy-how, what and when: report from an international consensus panel. *BJU Int.* **113**, 854–863 (2014).
8. Yesudas, S. S. et al. Percutaneous real-time ultrasound-guided renal biopsy performed solely by nephrologists: a case series. *Indian J. Nephrol.* **20**, 137–141 (2010).
9. Munoz, A. T. et al. Percutaneous renal biopsy of native kidneys: efficiency, safety and risk factors associated with major complications. *Arch. Med. Sci.* **7**, 823–831 (2011).
10. Whittier, W. L. & Korbet, S. M. Timing of complications in percutaneous renal biopsy. *J. Am. Soc. Nephrol.* **15**, 142–147 (2004).
11. Madaio, M. P. Renal biopsy. *Kidney Int.* **38**, 529–543 (1990).
12. Korbet, S. M., Volpini, K. C. & Whittier, W. L. Percutaneous renal biopsy of native kidneys: a single-center experience of 1,055 biopsies. *Am. J. Nephrol.* **39**, 153–162 (2014).
13. Schiavon, L. H. O. et al. Computed tomography-guided percutaneous biopsy of abdominal lesions: indications, techniques, results, and complications. *Radio. Bras.* **51**, 141–146 (2018).
14. Braak, S. J. et al. 3D cone-beam CT guidance, a novel technique in renal biopsy-results in 41 patients with suspected renal masses. *Eur. Radio.* **22**, 2547–2552 (2012).

15. Garnon, J. et al. Evaluation of percutaneous biopsies of renal masses under MRI-guidance: a retrospective study about 26 cases. *Eur. Radio.* **25**, 617–623 (2015).
16. Wang, Z. J., Westphalen, A. C. & Zagoria, R. J. CT and MRI of small renal masses. *Br. J. Radio.* **91**, 20180131 (2018).
17. Huang, D. et al. Optical coherence tomography. *Science* **254**, 1178–1181 (1991).
18. Barwari, K. et al. Advanced diagnostics in renal mass using optical coherence tomography: a preliminary report. *J. Endourol.* **25**, 311–315 (2011).
19. Yan, F. et al. Optical coherence tomography for multicellular tumor spheroid category recognition and drug screening classification via multi-spatial-superficial-parameter and machine learning. *Biomed. Opt. Express* **15**, 2014–2047 (2024).
20. Yan, F. et al. Polarization-sensitive optical coherence tomography for renal tumor detection in ex vivo human kidneys. *Opt. Lasers Eng.* **173**, 107900 (2024).
21. Israelsen, N. M. et al. Real-time high-resolution mid-infrared optical coherence tomography. *Light Sci. Appl.* **8**, 11 (2019).
22. Wang, C. et al. Forward optical coherence tomography endoscope for percutaneous nephrostomy guidance. In *Advanced Biomedical and Clinical Diagnostic and Surgical Guidance Systems XIX* (*SPIE BiOS*, 2021).
23. Wang, C. et al. Deep-learning-aided forward optical coherence tomography endoscope for percutaneous nephrostomy guidance. *Biomed. Opt. Express* **12**, 2404–2418 (2021).
24. Yuan, W. et al. Robust and fast characterization of OCT-based optical attenuation using a novel frequency-domain algorithm for brain cancer detection. *Sci. Rep.* **7**, 44909 (2017).
25. Wang, C. et al. Laparoscopic optical coherence tomography system for 3D bladder tumor detection. In *Advanced Photonics in Urology* (International Society for Optics and Photonics, 2021).
26. Wang, C. et al. Computer-aided Veress needle guidance using endoscopic optical coherence tomography and convolutional neural networks. *J. Biophotonics* **15**, e202100347 (2022).
27. Wang, C. et al. Epidural anesthesia needle guidance by forward-view endoscopic optical coherence tomography and deep learning. *Sci. Rep.* **12**, 9057 (2022).
28. Cui, S. et al. Needle size and the risk of kidney biopsy bleeding complications. *Kidney Int. Rep.* **1**, 324–326 (2016).
29. Marchand, E. W., *Gradient index optics*. 1978, New York: Academic Press. x, 166 p.
30. Wobker, S. E. & Williamson, S. R. Modern pathologic diagnosis of renal oncocytoma. *J. Kidney Cancer VHL* **4**, 1–12 (2017).
31. Faber, D. J. et al. Quantitative measurement of attenuation coefficients of weakly scattering media using optical coherence tomography. *Opt. Express* **12**, 4353–4365 (2004).
32. Gong, P. J. et al. Parametric imaging of attenuation by optical coherence tomography: review of models, methods, and clinical translation. *J. Biomed. Opt.* **25**, 1–34 (2020).
33. Scolaro, L. et al. Parametric imaging of the local attenuation coefficient in human axillary lymph nodes assessed using optical coherence tomography. *Biomed. Opt. Express* **3**, 366–379 (2012).
34. Cauberg, E. C. C. et al. Quantitative measurement of attenuation coefficients of bladder biopsies using optical coherence tomography for grading urothelial carcinoma of the bladder. *J. Biomed. Opt.* **15**, 066013 (2010).
35. Rodriguez, C. L. R. et al. Decreased light attenuation in cerebral cortex during cerebral edema detected using optical coherence tomography. *Neurophotonics* **1**, 025004 (2014).
36. Badre, A. & Pan, C. L. Explainable multi-task learning improves the parallel estimation of polygenic risk scores for many diseases through shared genetic basis. *Plos Comput. Biol.* **19**, e1011211 (2023).
37. Badre, A. & Pan, C. L. LINA: a linearizing neural network architecture for accurate first-order and second-order interpretations. *IEEE Access* **10**, 36166–36176 (2022).
38. Selvaraju, R. R. et al. Grad-CAM: visual explanations from deep networks via gradient-based localization. *Int. J. Comput. Vis.* **128**, 336–359 (2020).
39. Muller, B. G. et al. Prostate cancer diagnosis: the feasibility of needle-based optical coherence tomography. *J. Med Imaging* **2**, 037501 (2015).
40. Zhao, Q. L. et al. Ex vivo determination of glucose permeability and optical attenuation coefficient in normal and adenomatous human colon tissues using spectral domain optical coherence tomography. *J. Biomed. Opt.* **17**, 105004 (2012).
41. Wagstaff, P. G. K. et al. Percutaneous needle based optical coherence tomography for the differentiation of renal masses: a pilot cohort. *J. Urol.* **195**, 1578–1584 (2016).

Acknowledgements

This work was supported by grants from the University of Oklahoma Health Sciences Center (3P30CA225520), Institutional Research Grant number IRG-19-142-01 from the American Cancer Society, the National Science Foundation (OIA-2132161, 2238648), the National Institute of Health (R01DK133717), the Oklahoma Shared Clinical and Translational Resources (NIGMS U54GM104938), the Oklahoma Center for the Advancement of Science and Technology (HR23-071), the medical imaging COBRE (P20 GM135009), and the Midwest Biomedical Accelerator Consortium (MBArC), an NIH Research Evaluation and Commercialization Hub (REACH). Histology service provided by the Tissue Pathology Shared Resource was supported in part by the National Institute of General Medical Sciences COBRE Grant P20GM103639 and National Cancer Institute Grant P30CA225520 of the National Institutes of Health. Financial support was provided by the OU Libraries' Open Access Fund.

Author contributions

Chen Wang: imaging system design and establishment, experiment, data acquisition, and writing. Haoyang Cui: CNN model development, data training, and testing. Qinghao Zhang: attenuation coefficient method development and testing. Paul Calle: CNN model optimization. Yuyang Yan: attenuation coefficient method optimization. Feng Yan: system calibration. Kar-Ming Fung: biopsy analysis and system scanner design. Sanjay G. Patel: system endoscopy design. Zhongxin Yu: pathology analysis. Sean Duguay: cancer diagnosis and instruction on imaging procedure. William Vanlandingham: system design and calibration. Ajay Jain: experiment and histology. Chongle Pan: project administration, supervision and instruction of deep learning work, and writing—review and editing. Qinggong Tang: funding acquisition, project administration, supervision and instruction of imaging work, and writing—review and editing.

Competing interests

The authors declare no competing interests.

Additional information

Supplementary information The online version contains supplementary material available at https://doi.org/10.1038/s44172-024-00254-9.

Correspondence and requests for materials should be addressed to Chongle Pan or Qinggong Tang.

Peer review information *Communications Engineering* thanks the anonymous reviewers for their contribution to the peer review of this work. Primary Handling Editors: Richard Colchester, Anastasiia Vasylchenkova, and Rosamund Daw.